Jet-Launching Structure Resolved Near the Supermassive Black Hole in M87

Sheperd S. Doeleman *et al.*

Science **338**, 355 (2012);
DOI: 10.1126/science.1224768

Jet-Launching Structure Resolved Near the Supermassive Black Hole in M87

Sheperd S. Doeleman,[1,2]* Vincent L. Fish,[1] David E. Schenck,[1,3]† Christopher Beaudoin,[1] Ray Blundell,[2] Geoffrey C. Bower,[4] Avery E. Broderick,[5,6] Richard Chamberlin,[7] Robert Freund,[3] Per Friberg,[8] Mark A. Gurwell,[2] Paul T. P. Ho,[9] Mareki Honma,[10,11] Makoto Inoue,[9] Thomas P. Krichbaum,[12] James Lamb,[13] Abraham Loeb,[2] Colin Lonsdale,[1] Daniel P. Marrone,[3] James M. Moran,[2] Tomoaki Oyama,[10] Richard Plambeck,[4] Rurik A. Primiani,[2] Alan E. E. Rogers,[1] Daniel L. Smythe,[1] Jason SooHoo,[1] Peter Strittmatter,[3] Remo P. J. Tilanus,[8,14] Michael Titus,[1] Jonathan Weintroub,[2] Melvyn Wright,[4] Ken H. Young,[2] Lucy M. Ziurys[3]

Approximately 10% of active galactic nuclei exhibit relativistic jets, which are powered by the accretion of matter onto supermassive black holes. Although the measured width profiles of such jets on large scales agree with theories of magnetic collimation, the predicted structure on accretion disk scales at the jet launch point has not been detected. We report radio interferometry observations, at a wavelength of 1.3 millimeters, of the elliptical galaxy M87 that spatially resolve the base of the jet in this source. The derived size of 5.5 ± 0.4 Schwarzschild radii is significantly smaller than the innermost edge of a retrograde accretion disk, suggesting that the M87 jet is powered by an accretion disk in a prograde orbit around a spinning black hole.

The compact central regions of some galaxies are so luminous that they outshine the combined output of all other energy sources in the galaxy. The small size and high power output of these active galactic nuclei (AGN) are most plausibly explained by the conversion of gravitational energy through accretion onto a supermassive black hole. These black holes have masses of $M \gtrsim 10^6\ M_\odot$ ($M_\odot$, solar mass), in contrast with lower-mass black holes ($M \lesssim 10\ M_\odot$) that result from the gravitational collapse of evolved stars. Many AGN produce powerful collimated jets of relativistic particles that can extend for hundreds and thousands of light-years, providing an important mechanism for redistributing matter and energy on large scales that affect galactic evolution (*1*). Jets are thought to form through magnetic acceleration processes located within the accretion flow or at the central black hole itself (*2*–*4*), but no observations to date have had the angular resolution required to detect and confirm structure on these scales for extragalactic jet sources. High-resolution radio interferometry of these sources at centimeter wavelengths is limited by optical depth effects that obscure the innermost accretion region. For these reasons, it remains unclear if jet formation requires a spinning black hole (*5*, *6*), and if so, whether jets are more likely to be formed when the orbital angular momentum of the accretion flow is parallel (prograde) or antiparallel (retrograde) to the black hole spin (*7*, *8*). To address these questions, we have assembled a very long baseline interferometry (VLBI) array operating at a wavelength of 1.3 mm, the Event Horizon Telescope (*9*), where AGN start to become optically thin and angular resolutions necessary to resolve the inner accretion disks of nearby AGN are obtained.

Using a distance to M87 of 16.7 ± 0.6 Mpc (*10*) and adopting the corresponding recent mass measurement of $(6.2 \pm 0.4) \times 10^9\ M_\odot$ (*11*), the Schwarzschild radius of the M87 black hole [$R_{SCH} = 2\ GM/c^2 = (5.9 \pm 0.4) \times 10^{-4}$ pc = $(1.9 \pm 0.12) \times 10^{15}$ cm (G, gravitational constant; c, speed of light)] subtends an angle of 7.3 ± 0.5 micro–arc sec, presenting us with the best known opportunity for studying the formation of relativistic jets on scales commensurate with the black hole and accretion disk. Radiating via synchrotron emission, the relativistic jet from M87 extends for hundreds of kiloparsecs and terminates in extended lobes of emission as it slows and interacts

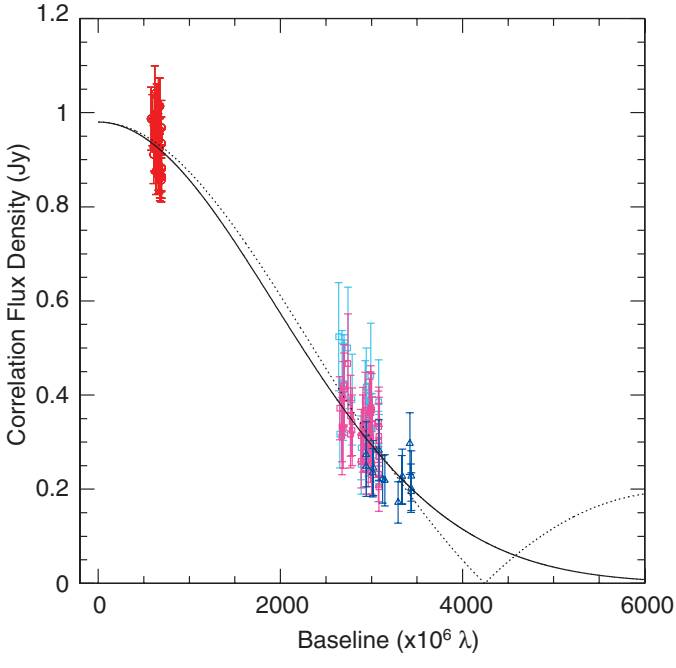

Fig. 1. Measuring the size of the M87 core with 1.3-mm VLBI. Correlated flux density data from 3 consecutive days of observing are plotted as a function of baseline length (in units of observing wavelength). The CARMA-SMT baselines are shown in red; the two baselines from CARMA dishes to the JCMT are shown in magenta and teal; the SMT-JCMT baseline is shown in blue. Calibration errors of 5% have been added in quadrature to the 1σ random errors associated with the incoherent fringe search performed on each baseline. The weighted least-squares best-fit circular Gaussian model is shown as a solid line and has a total flux density of 0.98 Jy and a FWHM size of 40.0 micro–arc sec. A hybrid model (dotted line) combines a circular Gaussian of the same size with a thin ring of diameter 40.0 micro–arc sec, which represents the expected shadow feature due to illumination of the central supermassive black hole from behind by a counterjet in M87. In the hybrid model, the Gaussian and ring components each contribute one-half of the flux density. On VLBI baselines shorter than the null spacing, the VLBI interferometric phase is zero, but on baselines beyond the null spacing, the phase is 180°.

[1]MIT Haystack Observatory, Off Route 40, Westford, MA 01886, USA. [2]Harvard Smithsonian Center for Astrophysics, 60 Garden Street, Cambridge, MA 02138, USA. [3]Steward Observatory, Arizona Radio Observatory, University of Arizona, 933 North Cherry Avenue, Tucson, AZ 85721–0065, USA. [4]Department of Astronomy, University of California Berkeley, Hearst Field Annex, Berkeley, CA 94720, USA. [5]Perimeter Institute, 31 Caroline Street, North Waterloo, Ontario N2L 2Y5, Canada. [6]Department of Physics and Astronomy, University of Waterloo, 200 University Avenue West, Waterloo, Ontario N2l 3G1, Canada. [7]Caltech Submillimeter Observatory, 111 Nowelo Street, Hilo, HI 96720, USA. [8]James Clerk Maxwell Telescope, Joint Astronomy Centre, 660 North A'ohoku Place University Park, Hilo, HI 96720, USA. [9]Academia Sinica Institute for Astronomy and Astrophysics, 11F Astronomy-Mathematics Building, National Taiwan University, No. 1, Roosevelt Road, Section 4 Taipei 10617, Taiwan, R.O.C. [10]National Astronomical Observatory of Japan, 2-21-1 Osawa, Mitaka, Tokyo 181-8588, Japan. [11]The Graduate University for Advanced Studies, Osawa, Mitaka, Tokyo 181-8588, Japan. [12]Max-Planck-Institut für Radioastronomie, Auf dem Hügel 69, 53121 Bonn, Germany. [13]Owens Valley Radio Observatory, California Institute of Technology, 100 Leighton Lane, Big Pine, CA 93513–0968, USA. [14]Netherlands Organisation for Scientific Research, Laan van Nieuw Oost-Indie 300, NL2509 AC The Hague, Netherlands.

*To whom correspondence should be addressed. E-mail: sdoeleman@haystack.mit.edu

†Present address: Department of Astrophysical and Planetary Sciences, University of Colorado at Boulder, 391 UCB, Boulder, CO 80309, USA.

with the intergalactic medium. Closer to the galaxy's core, on a scale of hundreds of parsecs, the radio jet is remarkably well collimated, with an opening angle of less than 5° (*12*), and is also clearly seen in the optical, ultraviolet, and x-ray (*13*, *14*), where the emission is primarily confined to knots along the central "spine" of the jet. VLBI observations at wavelengths ranging from 3.5 mm to 20 cm show that the jet opening angle, delineated by edge brightening in the outflow, continually increases as the core is approached, reaching ~60° within 1 milli–arc sec of the core (*15*–*19*). This wide opening angle is a signature of the launch point for a magnetohydrodynamically (MHD) powered jet that has not yet had time to collimate (*2*), and it identifies the VLBI core as the most likely site of the central black hole.

We observed M87 over 3 consecutive days with a 1.3-mm wavelength VLBI array consisting of four telescopes at three geographical locations: the James Clerk Maxwell Telescope (JCMT) on Mauna Kea in Hawaii, the Arizona Radio Observatory's Submillimeter Telescope (SMT) in Arizona, and two telescopes of the Combined Array for Research in Millimeter-wave Astronomy (CARMA, located ~60 m apart) in California. On Mauna Kea, the JCMT partnered with the Submillimeter Array (SMA), which housed the hydrogen maser atomic frequency standard and wideband VLBI recording systems; the SMT and CARMA were similarly equipped. These special-purpose systems allowed two frequency bands, each of 512 MHz bandwidth, to be sampled at 2-bit precision and recorded at an aggregate rate of 4 gigabits/s. The two bands, labeled "low" and "high," were centered on 229.089 GHz and 229.601 GHz, respectively. Data recorded at all sites were shipped to the MIT Haystack Observatory for processing on the Mark4 VLBI correlator. Once correlated, data for each VLBI scan (typically 10 min) were corrected for coherence losses due to atmospheric turbulence and were searched for detections using established algorithms tailored for high-frequency observations (*20*). M87 was clearly detected each day on all VLBI baselines, and the interferometric data were then calibrated to flux density units (*20*).

Clear detections on the long baselines to Hawaii (CARMA-JCMT and SMT-JCMT) represent the highest angular resolution observations of M87 reported in any waveband, and when combined with the CARMA-SMT baseline data, they provide a robust means to measure the size of the M87 core. The baseline between the two CARMA antennas corresponds to angular scales of ~4 arc sec and is sensitive to extended and much larger-scale jet structure; these data were thus used to refine the calibration of the antennas but were excluded from the analysis of the core component. To extract a size for the core, we fitted a two-parameter circular Gaussian model to the 1.3-mm VLBI data, deriving a total flux density and full width at half maximum (FWHM) size for each day of observations. Sizes and flux densities fit separately for each day are consistent with each other at the 3σ level, indicating no significant variation in the 1.3-mm core structure over the 3 days of observation (fig. S4). When data from all 3 days are combined, the weighted least-squares best-fit model for the compact component results in a flux density of 0.98 ± 0.04 Jy and a FWHM of 40 ± 1.8 micro–arc sec (3σ errors) (Fig. 1). The conversion to units of Schwarzschild radius yields a value of 5.5 ± 0.4 R_{SCH} (1σ errors), where the errors are dominated by uncertainties in the distance to M87 and the black hole mass. We adopt the circular Gaussian size derived using data from all 3 days for subsequent discussion.

Our VLBI observations cannot be used to fix the absolute position of this Gaussian component; however, in the case of M87, there is compelling evidence that this ultracompact 1.3-mm emission is in immediate proximity to the central supermassive black hole. Measurements of the jet width starting tens of R_{SCH} from the core and extending to core-separations of more than 10^4 R_{SCH} are well fit by a parabola-like collimating profile (*19*) (Fig. 2). This fit matches similar profiles of general relativistic MHD (GRMHD) jet simulations (*21*, *22*). When extrapolated to small scales, the empirical profile intersects the 1.3-mm emission component size within one R_{SCH} of the jet base. Because the angle of the M87 jet axis to our line of sight is estimated to be within the range of 15° to 25° (*23*), the deprojected distance of this intersection point from the jet base lies in the range of 2.5 to 4 R_{SCH}. A second method of locating the 1.3-mm emission derives from observations of the position shift of the M87 core as a function of wavelength. Multiwavelength astrometric VLBI observations (15 cm to 7 mm) confirm that the absolute position of the core moves asymptotically toward the jet base with a $\nu^{-0.94}$ dependence (*23*). Extrapolation to 1.3 mm wavelength places the 1.3-mm VLBI component coincident with the jet base to within the uncertainty of the core-shift relation, which is ~1.5 R_{SCH}. In isolation, these observational trends would be unable to clearly link the jet base with the central engine. In blazar sources, for example, the relativistic jets are closely aligned to our line of sight, and the jet base is illuminated hundreds of thousands of R_{SCH} from the central engine (*24*). In contrast, M87 is now the only known case where the jet base has a size (~5.5 R_{SCH}) that is consistent with scales on which energy is extracted from the black hole and accretion disk to feed the jet (*2*). It is thus most natural to spatially associate the 1.3-mm VLBI component with the central engine, further guided by GRMHD simulations (*21*) that exhibit jet widths, within a few R_{SCH} of the black hole, that match the 1.3-mm VLBI size (Fig. 2). In M87, the favorable geometry of a misaligned jet and increased transparency of the synchrotron emission at millimeter wavelengths (*25*) have allowed us direct access to the innermost central engine with 1.3-mm VLBI.

The most plausible mechanisms for powering extragalactic jets involve conversion of the black hole rotational energy through the Blandford-Znajek (BZ) process (*3*), whereby magnetic field lines cross the black hole event horizon and launch

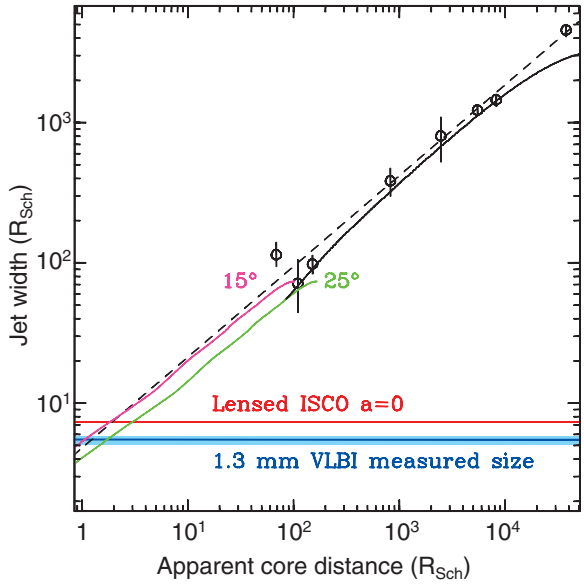

Fig. 2. Width profile of the M87 jet as a function of distance from the core. Measurements of the jet opening angle from the literature (*33*) were converted to projected jet width and fit with a power law (dashed black line) of the form $\theta \propto r^{\beta}$, where θ is jet width and r is separation from the core. The best fit $\theta \propto r^{0.69}$ indicates a parabola-like profile for the jet, with collimation increasing at larger distances as expected from MHD theory, and is in agreement with recent detailed measurements of the M87 jet profile (*19*). The dark blue horizontal line indicates the size reported in this paper, with the light blue band corresponding to 1σ uncertainties. To estimate the position relative to the central black hole, we extrapolated the power law fit, which intersects the 1.3-mm VLBI size at an apparent core distance of ~1 R_{SCH}. GRMHD models, tailored to simulate jet emission from the black hole out to distances of ~100 R_{SCH}, are shown as the solid magenta and green lines for jet axis angles to our line of sight of 15° and 25°, respectively (*21*). These close-in simulations also intersect the 1.3-mm VLBI size between 1 and 2 R_{SCH} from the black hole. For comparison and illustration, jet width values derived from a separate GRMHD simulation of the larger-scale M87 jet (*22*) are shown as a solid black line for distances larger than ~100 R_{SCH}. The red horizontal line indicates the apparent size of the ISCO for a nonspinning black hole when strong gravitational lensing effects near the black hole are properly accounted for (*20*).

Poynting flux–dominated outflows. The inner portion of the accretion disk is not only the source of the magnetic fields threading the black hole, but also launches a disk-wind via the Blandford-Payne (BP) mechanism (*4*), which serves to collimate the jet. This BZ/BP combination forms a spine/sheath morphology, in which a narrow, electromagnetic, and initially nonradiative jet from the black hole is surrounded by a slower and quickly mass-loaded outflow originating from the inner disk (*6*, *26*). In the case of M87, the broad opening angle and existence of a counterjet (*17*, *18*) indicate that the dominant contribution to the 1.3-mm VLBI emission is from the slower-moving sheath, anchored within the accretion disk (*6*). In this model of jet genesis, which we adopt here, the critical size scale associated with the jet footprint is the innermost stable circular orbit (ISCO) of the black hole, within which matter quickly plunges to the event horizon. The ISCO marks the peak density and rotational speed of the accretion flow (*27*) and is the location where particles are most efficiently accelerated from the disk (*5*) and begin to radiate. Strong beaming effects, which might produce small and high-brightness features unrelated to the ISCO, are not expected to be a factor on the scales probed by the 1.3-mm VLBI observations, because the detection of a counterjet in M87 and the parabolic profile of the jet both indicate that the outflow near the black hole is subrelativistic.

Based on this understanding of the M87 jet, and taking the 1.3-mm VLBI size as the ISCO diameter, we estimated the black hole spin and determined whether the accretion disk orbits in a prograde or retrograde sense. This is possible because the intrinsic ISCO diameter (D_{ISCO}) is sensitively dependent on black hole spin, with a value of $D_{ISCO} = 6\ R_{SCH}$ for a nonspinning (Schwarzschild) black hole [spin (a) = 0], and ranging from $D_{ISCO} = 9\ R_{SCH}$ to $D_{ISCO} = 1\ R_{SCH}$ for retrograde and prograde orbits, respectively, around a maximally spinning (Kerr) black hole (a = 1). Strong lensing effects due to the Kerr spacetime metric near the rotating black hole magnify the apparent size of the ISCO, with the relationship between observed ISCO size and black hole spin shown in Fig. 3 (*20*, *28*). The measured 1.3-mm VLBI size corresponds to a prograde ISCO around a black hole with $a > 0.2$ (3σ). This result explicitly excludes the possibility of a retrograde ISCO orbit in the accretion flow, because all such orbits would be larger than the core size derived here. The smallest possible retrograde ISCO orbit would present an apparent diameter of 7.35 R_{SCH}, which is more than 4σ larger than the observed size. This result is consistent with generally accepted theories that the spin axes of the accretion disk and black hole will be brought into alignment through gradual angular momentum transfer from the orbiting disk (*29*).

As the sensitivity and resolution of the 1.3-mm VLBI array improve, modeling of the data can move beyond simple Gaussian distributions to physically motivated models that include accretion physics, relativistic beaming, and full GR ray tracing. Recent modeling of the M87 jet on Schwarzschild radius scales indicates that in many cases, emission from a counterjet will illuminate the black hole from behind, creating a bright feature at the last photon orbit (*25*, *30*). The relatively dim region interior to this ring is known as the black hole shadow or silhouette, and its dimensions are determined by black hole mass, spin, and inclination of the spin axis (*31*). Over a wide range of spin and inclination, the last photon ring of emission has a diameter of $D_{RING} = 5.2\ R_{SCH}$, so that fitting for the ring size yields an estimate of the black hole mass (*32*). The presence of such a shadow feature is not ruled out by the 1.3-mm VLBI data presented here, which can be well fitted by a hybrid model combining a circular Gaussian representing jet emission launched from the ISCO, with a uniform annular ring at the last photon orbit (Fig. 1). Although the current VLBI array cannot be used to meaningfully constrain this more complex model, there are two distinguishing characteristics of this hybrid approach that can be readily tested with future 1.3-mm VLBI arrays. The first is a predicted null in correlated flux density near baseline lengths of $4.5 \times 10^9\ \lambda$ (λ, observing wavelength), and the second is a 180° flip in interferometric phase between VLBI baselines on either side of this null.

It is increasingly clear that strong gravity effects can dominate observed AGN structure on the scales accessible with short-wavelength VLBI. Included among these effects is the spin-dependent ISCO period, which ranges from 5 days (a = 1) to 1 month (a = 0) for the mass of the M87 black hole. The consistency of the 1.3-mm VLBI sizes presented here, spanning 3 days of observation, does not reflect dramatic structural changes in the jet that might be expected because of accretion disk inhomogeneity for a black hole spinning near the maximum rate (fig. S4). More-sensitive searches for such periodic features in the jet launch region can be carried out with the full Event Horizon Telescope. In general, this work signals that Earth-sized 1.3-mm VLBI networks are now able to provide angular resolutions that link observations of compact objects dominated by strong-field GR to outflows on the largest galactic scales.

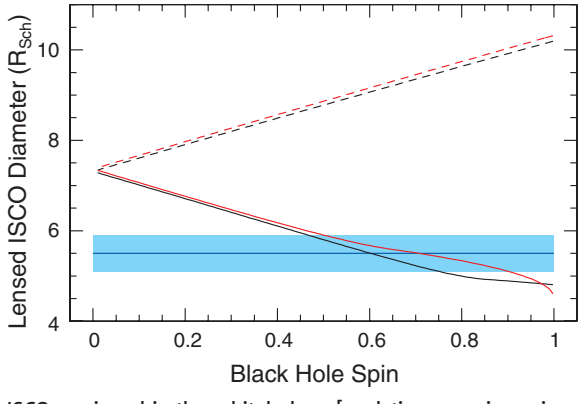

Fig. 3. Diameter of the ISCO for a black hole of arbitrary spin. The apparent diameter of the ISCO due to the strong gravitational lensing near the black hole was computed using ray-tracing algorithms through Kerr spacetime (*34*, *35*). Two scenarios are shown. The black curve is the apparent diameter of an opaque sphere whose radius coincides with the ISCO and is viewed along the spin axis of the black hole. This distribution approximates a thick accretion disk, which is appropriate for M87. The red curve is the apparent diameter for a ring of emission at the ISCO as viewed in the orbital plane [analytic expressions given in (*20*)]. Solid lines show prograde ($a > 0$) orbits, and dashed lines show retrograde ($a < 0$) orbits. The 1.3-mm VLBI size derived in this work is shown as a horizontal blue line with a cyan band marking the ±1σ uncertainty. The 3σ upper limit on the 1.3-mm VLBI size corresponds to a lower limit on the black hole spin of ($a > 0.2$).

References and Notes

1. D. Richstone *et al.*, *Nature* **395**, A14 (1998).
2. D. L. Meier, S. Koide, Y. Uchida, *Science* **291**, 84 (2001).
3. R. D. Blandford, R. L. Znajek, *Mon. Not. R. Astron. Soc.* **179**, 433 (1977).
4. R. D. Blandford, D. G. Payne, *Mon. Not. R. Astron. Soc.* **199**, 883 (1982).
5. J.-P. De Villiers, J. F. Hawley, J. H. Krolik, S. Hirose, *Astrophys. J.* **620**, 878 (2005).
6. J. McKinney, *Mon. Not. R. Astron. Soc.* **368**, 1561 (2006).
7. D. Garofalo, D. A. Evans, R. M. Sambruna, *Mon. Not. R. Astron. Soc.* **406**, 975 (2010).
8. A. Tchekhovskoy, J. McKinney, *Mon. Not. R. Astron. Soc.* **423**, 55 (2012).
9. D. Clery, *Science* **335**, 391 (2012).
10. J. Blakeslee *et al.*; The ACS Fornax Cluster Survey, *Astrophys. J.* **694**, 556 (2009).
11. K. Gebhardt *et al.*, *Astrophys. J.* **729**, 119 (2011).
12. J. A. Biretta, F. Zhou, F. N. Owen, *Astrophys. J.* **447**, 582 (1995).
13. E. S. Perlman, J. A. Biretta, W. B. Sparks, F. D. Macchetto, J. P. Leahy, *Astrophys. J.* **551**, 206 (2001).
14. H. L. Marshall *et al.*, *Astrophys. J.* **564**, 683 (2002).
15. W. Junor, J. A. Biretta, M. Livio, *Nature* **401**, 891 (1999).
16. T. P. Krichbaum *et al.*, *J. Phys. Conf. Ser.* **54**, 328 (2006).
17. C. Ly, R. C. Walker, W. Junor, *Astrophys. J.* **660**, 200 (2007).
18. Y. Y. Kovalev, M. L. Lister, D. C. Homan, K. I. Kellermann, *Astrophys. J.* **668**, L27 (2007).
19. K. Asada, M. Nakamura, *Astrophys. J.* **745**, L28 (2012).
20. See the supplementary materials on *Science* Online.
21. J. C. McKinney, R. D. Blandford, *Mon. Not. R. Astron. Soc.* **394**, L126 (2009).
22. J. Gracia, N. Vlahakis, I. Agudo, K. Tsinganos, S. V. Bogovalov, *Astrophys. J.* **695**, 503 (2009).
23. K. Hada *et al.*, *Nature* **477**, 185 (2011).
24. A. P. Marscher *et al.*, *Nature* **452**, 966 (2008).
25. A. E. Broderick, A. Loeb, *Astrophys. J.* **697**, 1164 (2009).
26. P. E. Hardee, *Astrophys. J.* **664**, 26 (2007).
27. C. P. Fragile, *Astrophys. J.* **706**, L246 (2009).
28. A. Broderick, A. Loeb, R. Narayan, *Astrophys. J.* **701**, 1357 (2009).

29. C. Gammie, S. Shapiro, J. McKinney, *Astrophys. J.* **602**, 312 (2004).
30. J. Dexter, J. C. McKinney, E. Agol, *Mon. Not. R. Astron. Soc.* **421**, 1517 (2012).
31. H. Falcke, F. Melia, E. Agol, *Astrophys. J.* **528**, L13 (2000).
32. T. Johannsen, D. Psaltis, *Astrophys. J.* **718**, 446 (2010).
33. J. A. Biretta, W. Junor, M. Livio, *New Astron. Rev.* **46**, 239 (2002).
34. A. E. Broderick, R. Blandford, *Mon. Not. R. Astron. Soc.* **342**, 1280 (2003).
35. A. E. Broderick, A. Loeb, *Mon. Not. R. Astron. Soc.* **367**, 905 (2006).

Acknowledgments: High-frequency VLBI work at the MIT Haystack Observatory is supported by grants from NSF. The Submillimeter Array is a joint project between the Smithsonian Astrophysical Observatory and the Academia Sinica Institute of Astronomy and Astrophysics. The Submillimeter Telescope is operated by the Arizona Radio Observatory (ARO). ARO is partially supported through the NSF University Radio Observatories (URO: grant AST-1140030) and ATI (grant AST-0905844) programs. The James Clerk Maxwell Telescope is operated by the Joint Astronomy Centre on behalf of the Science and Technology Facilities Council of the UK, the Netherlands Organisation for Scientific Research, and the National Research Council of Canada. Funding for ongoing CARMA development and operations is supported by NSF and the CARMA partner universities. We thank the NASA Geodesy Program for loan of the CARMA Hydrogen Maser; J. Test, P. Yamaguchi, G. Reiland, J. Hoge, and M. Hodges for technical assistance; the staff at all participating facilities; J. Gracia and J. McKinney for providing jet simulation data used in this work; and Xilinx, Inc., for equipment donations. Data used in this paper are available in the supplementary materials.

Supplementary Materials
www.sciencemag.org/cgi/content/full/science.1224768/DC1
Methods
Figs. S1 to S4
Tables S1 and S2
References (*36*–*40*)

16 May 2012; accepted 13 September 2012
Published online 27 September 2012;
10.1126/science.1224768

Self-Assembled Colloidal Superparticles from Nanorods

Tie Wang,[1] Jiaqi Zhuang,[1] Jared Lynch,[1] Ou Chen,[1] Zhongliang Wang,[1] Xirui Wang,[1] Derek LaMontagne,[1] Huimeng Wu,[1] Zhongwu Wang,[2] Y. Charles Cao[1]*

Colloidal superparticles are nanoparticle assemblies in the form of colloidal particles. The assembly of nanoscopic objects into mesoscopic or macroscopic complex architectures allows bottom-up fabrication of functional materials. We report that the self-assembly of cadmium selenide–cadmium sulfide (CdSe-CdS) core-shell semiconductor nanorods, mediated by shape and structural anisotropy, produces mesoscopic colloidal superparticles having multiple well-defined supercrystalline domains. Moreover, functionality-based anisotropic interactions between these CdSe-CdS nanorods can be kinetically introduced during the self-assembly and, in turn, yield single-domain, needle-like superparticles with parallel alignment of constituent nanorods. Unidirectional patterning of these mesoscopic needle-like superparticles gives rise to the lateral alignment of CdSe-CdS nanorods into macroscopic, uniform, freestanding polymer films that exhibit strong photoluminescence with a striking anisotropy, enabling their use as downconversion phosphors to create polarized light-emitting diodes.

Directional bonding interactions dictate the structural complexity and functional specificity of naturally occurring materials at all length scales (*1*–*4*). On the nanometer scale, anisotropic nanoparticles are used to design directional bonding interactions through shape-specific (*3*–*5*) and surface-specific functionalization (*6*, *7*). Because anisotropic nanoparticles exhibit shape-dependent physical and chemical properties (*8*, *9*), the self-assembly of these nanoparticles can lead to metamaterials with important collective properties (*3*) such as spin-dependent electron transport (*10*), vibrational coherence (*11*), enhanced conductivity (*12*), and tandem catalysis (*13*). We report that anisotropy-driven self-assembly of CdSe-CdS core-shell semiconductor nanorods produces three-dimensional (3D) colloidal superparticles with multiple well-defined supercrystalline domains or needle-like superparticles with a single supercrystalline domain. The needle-like superparticles can be unidirectionally aligned and further assembled into centimeter-scale, uniform, freestanding polymer films, exhibiting a photoluminescence (PL) anisotropy ratio larger than that of single CdSe-CdS nanorods.

Colloidal CdSe-CdS superparticles were prepared using a previously described method with minor modifications (*14*), including two major steps: (i) synthesis of water-soluble nanorod micelles and (ii) growth of superparticles from nanorod micelles in an aqueous solution of ethylene glycol (Fig. 1A). We used highly fluorescent CdSe-CdS nanorods primarily capped with octylamine and octadecylphosphonic acid (ODPA), prepared via a literature method (*15*, *16*), as precursors for making nanorod micelles (figs. S1 to S3). In a typical superparticle synthesis (*17*), a clear nanorod-micelle aqueous solution was prepared by mixing a chloroform solution of CdSe-CdS nanorods with length $l = 28.0 \pm 1.5$ nm and diameter $d = 6.7 \pm 0.3$ nm (10 mg/ml, 1 ml) with an aqueous solution (1 ml) containing varying amounts of dodecyl trimethylammonium bromide (DTAB), followed by bubbling Ar to evaporate chloroform. Under vigorous stirring, the nanorod micelle solution was injected into a three-neck flask with ethylene glycol (5.0 ml), causing the decomposition of nanorod micelles as a result of the loss of DTAB molecules into the growth solution. This led to the aggregation of nanorods and the eventual formation of superparticles (Fig. 1A). After stirring for 10 min, an aqueous solution of dithiol-functionalized Tween-20 (0.1 mM, 1.0 ml) was added into the growth solution to stabilize the superparticles (*14*). The resulting superparticles were isolated and purified by centrifugation and redispersed in polar solvents (such as water, ethanol, and ethylene glycol) at a variety of concentrations.

Previous studies have shown that the amount of DTAB affects the kinetics of superparticle formation from isotropic spherical nanocrystals and thus can be used to achieve a size-controlled synthesis of superparticles (*18*), and we apply this to the synthesis of superparticles from nanorods. Accordingly, we have prepared CdSe-CdS superparticles with an average size ranging from 180 ± 23 nm to 1100 ± 150 nm by varying the amount of DTAB in nanorod micelle solutions (*18*). Low-magnification transmission electron microscope (TEM) images show that the resulting superparticles are nearly spherical (fig. S4), whereas higher-magnification images from tilting experiments reveal that these superparticles exhibit multiple supercrystalline domains with configurations and sizes that are dependent on the total number (N) of constituent nanorods inside each superparticle (Fig. 1, B to P, and fig. S5).

When N is less than ~80,000, superparticles typically exhibit a morphology of double-domed cylinders, wherein the cylindrical domain occupies a volume larger than that of the corresponding domes (Fig. 1, B to K). The cylindrical domain adopts a lamellar structure that consists of stacked multilayer disks formed from nanorods via lateral association, where the thickness of each disk is consistent with the length of a single nanorod. With an increase of N, the radius of the cylindrical domain increases, and so does the number of stacked-disk monolayers but with some fluctuations (Fig. 1, B to K). For example, the superparticle shown in Fig. 1G possesses more constituent rods than that shown in Fig. 1F, but the cylindrical domain of the superparticle in Fig. 1F has one more stacked-disk monolayer. When N is larger than ~80,000, CdSe-CdS superparticles appear as either irregular-multidomain particles (Fig. 1, L, M, and O) or double-domed cylinders (Fig. 1, N and P).

TEM tilting experiments further reveal that the domes in a double-domed cylinder typically consist of three supercrystalline domains together

[1]Department of Chemistry, University of Florida, Gainesville, FL 32611, USA. [2]Cornell High Energy Synchrotron Source, Wilson Laboratory, Cornell University, Ithaca, NY 14853, USA.

*To whom correspondence should be addressed. E-mail: cao@chem.ufl.edu